Eur. Phys. J. A **12**, 421–433 (2001)

THE EUROPEAN PHYSICAL JOURNAL A

Testing Dirac-Brueckner models in collective flow of heavy-ion collisions

T. Gaitanos[1], C. Fuchs[2,a], H.H. Wolter[1], and A. Faessler[2]

[1] Sektion Physik der Universität München, Am Coulombwall 1, D-85748 Garching, Germany
[2] Institut für Theoretische Physik der Universität Tübingen, Auf der Morgenstelle 14, D-72076 Tübingen, Germany

Received: 8 January 2001 / Revised version: 31 October 2001
Communicated by P. Schuck

Abstract. We investigate differential in-plane and out-of-plane flow observables in heavy-ion reactions at intermediate energies from 0.2–2 AGeV within the framework of relativistic BUU transport calculations. The mean field is based on microscopic Dirac-Brueckner-Hartree-Fock (DB) calculations. We apply two different sets of DB predictions, those of ter Haar and Malfliet and more recent ones from the Tübingen group, which are similar in general but differ in details. The latter DB calculations exclude spurious contributions from the negative-energy sector to the mean field which results in a slightly softer equation of state and a less repulsive momentum dependence of the nucleon-nucleus potential at high densities and high momenta. For the application to heavy-ion collisions in both cases non-equilibrium features of the phase space are taken into account on the level of the effective interaction. The systematic comparison to experimental data favours the less repulsive and softer model. Relative to non-relativistic approaches one obtains larger values of the effective nucleon mass. This produces a sufficient amount of repulsion to describe the differential flow data reasonably well.

PACS. 25.75.-q Relativistic heavy-ion collisions – 25.75.Ld Collective flow – 25.70.Mn Projectile and target fragmentation – 21.65.+f Nuclear matter

1 Introduction

Relativistic heavy-ion collisions have been extensively investigated to determine the nuclear equation of state (EOS) far away from saturation and at finite temperature, using semi-classical transport models of the Boltzmann type [1,2]. The nuclear EOS which enters into a transport description via density and momentum-dependent mean fields has mostly been based on phenomenological considerations by adjusting the parameters to nuclear-matter saturation properties and to the momentum dependence of the empirical nucleon-nucleus optical potential [3]. Such parametrisations, as, *e.g.*, Skyrme-type potentials [4], imply different extrapolations to high and low densities and high momenta, which should be tested in heavy-ion reactions. Thus, there have been many efforts to determine the density and momentum dependence of the nuclear mean field by studying the different aspects of the collective flow in intermediate energy heavy-ion collisions between 0.1–2 AGeV (SIS energies) [4–15].

On the other hand, it is well known that hadrons generally change their properties in the medium. This basic feature is already incorporated in the simplest version of a relativistic hadronic model for nuclear matter, namely linear Quantum Hadron Dynamics (QHD) [16], where the effective nucleon mass drops with density. To obtain a reasonable compressibility, scalar self-interaction terms are introduced and finite nuclei are well described [17]. At much higher densities, *i.e.* for the description of neutron stars, also non-linear terms of the vector mean field are required [18]. These different treatments reflect the inherent uncertainties in density extrapolations away from the saturation point. More recent and systematic approaches try to fix the relevant terms, *e.g.* by density functional expansions of generalised QHD Lagrangians [19,20] which effectively incorporate the basic features of chiral symmetry and its breaking. However, predictions for high densities remain questionable since effective field theory provides a low-density expansion scheme valid in the vicinity of the nuclear saturation point and below [20,21].

An alternative approach to the density and momentum dependence of the mean field is provided by microscopic many-body models. Here the nucleon-nucleon (NN) interaction is fixed by free NN-scattering and no parameters are adjusted to the nuclear-matter problem. In the relativistic Dirac-Brueckner-Hartree-Fock (DB) approach [22–27] the NN-interaction is based on modern one-boson-exchange (OBE) potentials [28] and the in-medium ladder diagrams are summed self-consistently. This approach de-

[a] e-mail: christian.fuchs@uni-tuebingen.de

scribes the nuclear-matter saturation properties very reasonably, albeit not perfectly. There exist good arguments why DB should be still reliable at higher densities. As pointed out in [29] the non-local structure of the OBE potentials accounts already effectively on the two-body level for some features of many-nucleon terms, *e.g.*, intermediate Δ-excitations, and higher-order effects cancel to large extent. Then the success of non-linear QHD Lagrangians can be understood in that these models parametrise phenomenologically the density dependence of the microscopic DB predictions [30]. However, the constraints from finite nuclei on the explicit form of the different fields are limited since the single-particle potential results from the cancellation of large scalar and vector potentials. Only the spin-orbit interaction allows to constrain the magnitude of the effective mass [17,19,27]. On the other hand, in energetic heavy-ion reactions scalar and vector fields are decoupled by their different Lorentz transformation properties, in the sense that they can be tested independently, and additional information on the structure of the potential can be obtained. Thus, within the DB framework there is a chance to attempt a *unified* description of different nuclear systems, *i.e.* free NN-scattering, nuclear matter, finite nuclei and heavy-ion collision.

However, relativistic Brueckner calculations are not straightforward and the approaches of various groups [23–26] are similar but differ in detail, depending on the solution techniques and the particular approximations made. In the present work we therefore want to study the DB predictions for the nuclear mean field in more detail in heavy-ion collisions. In previous studies [14,15] a qualitative agreement with collective flow observables has been found. Recently more detailed experiments have been performed for differential components of the collective flow [31]. In particular, the rapidity and transverse momentum dependence of collective flow has attracted much theoretical interest because of their strong sensitivity to the momentum dependence of the nuclear mean field [12]. Here we test the self-energies, *i.e.* the nuclear EOS, from two different DB calculations, from ter Haar and Malfliet [24] and from a more recent study performed by the Tübingen group [25, 26].

In heavy-ion collisions a further difficulty arises due to the non-equilibrium features of the phase space configurations. This has been discussed extensively in refs. [14,15]. In a fully consistent treatment, one would have to solve the coupled set of DB equations for the effective interaction in non-equilibrium nuclear-matter configurations simultaneously with the kinetic equations for the evolution of a phase space distribution [23]. However, such a procedure has not been realized yet, and further approximations are necessary in heavy-ion collisions. In the local density approximation (LDA) the nuclear-matter mean fields are directly used in the transport calculation. However, this approximation is not reliable enough at intermediate energies, because the local momentum space is highly anisotropic during a large part of the heavy-ion collision [15,32,33]. A better approximation is the colliding nuclear-matter (CNM) approach, where the phase space anisotropies are parametrised by two inter-penetrating nuclear-matter currents, *i.e.* the local momentum space is given by two Fermi spheres, or covariant Fermi ellipsoids, with given Fermi momenta and a relative velocity [34]. In ref. [34] a method was developed to extrapolate nuclear-matter DB results to CNM configurations. The CNM self-energies are applied to heavy-ion collisions in the Local (phase space) Configuration Approximation (LCA) [14,15,35], where the anisotropic phase space is locally parametrised by a CNM configuration. In this paper, the LCA approximation is only briefly discussed, details can be found in [14,15,34]. We shall discuss the density and momentum dependence of the DB mean fields and their application to the CNM approximation in terms of an effective equation of state [36].

This paper is organised as follows: The DB formalism and the different DB models are reviewed in sect. 2. The CNM approximation is discussed in sect. 3. In sect. 4 the transport equation and their numerical realization is outlined. Then we discuss the density and momentum dependence of the DB mean fields in ground-state nuclear matter, and the LCA approximation for anisotropic phase space configurations in heavy-ion collisions. Section 5 contains the results of transport calculations based on the DB mean fields of refs. [24,26] in the LCA approximation. We compare different components of collective flow with respect to its energy, centrality, transverse momentum and rapidity dependence. It is found that both models are able to qualitatively describe the experimental results, but in details one finds model dependences on the collective flow observables.

2 The DB approach

Brueckner theory provides a microscopic model which accounts for two-body correlations in the ladder approximation in medium in the Bethe-Goldstone or the Bethe-Salpeter equation in the relativistic case,

$$\mathcal{T} = V + i \int VGG\mathcal{T} \quad . \tag{1}$$

The correlations of the Green functions, or wave functions respectively, are shifted to the effective in-medium interaction, *i.e.* the $\mathcal{T}$-matrix (or $\mathcal{G}$-matrix) [23]. The in-medium propagator obeys a Dyson equation

$$G = G^0 + \int G^0 \Sigma G \tag{2}$$

and is dressed by a self-energy Σ obtained in Hartree-Fock approximation from the $\mathcal{T}$-matrix

$$\Sigma = -i \int \mathcal{T} G \quad . \tag{3}$$

The coupled set of equations (1)-(3) has to be solved self-consistently. In this procedure the bare interaction V, iterated in the Bethe-Salpeter equation, is sandwiched

between dressed in-medium spinors. This feature is absent in non-relativistic approaches and introduces an additional density dependence which is responsible for the significantly improved saturations properties compared to non-relativistic $\mathcal{G}$-matrix calculations [37,38]. The non-relativistic Brueckner approach leads to too large saturation densities (*e.g.*, $\rho_{\rm sat} = 0.2$ fm^{-3} in [37] and $\rho_{\rm sat} = 0.24$ fm^{-3} in [38]) and predicts a rather small compressibility ($K = 180$ MeV in [35,37]). The introduction of 3-body forces can in principle improve on this in the non-relativistic case [38].

In contrast to the phenomenological approaches like QHD [16] and to effective field theory [19,21] this approach is essentially parameter free. The only free parameters are those of the NN-interaction, namely those of the realistic OBE potentials, which are fixed by the free-scattering problem [28]. The success of the DB model indicates that it already accounts for the most important set of diagrams to describe nuclear matter. A further inclusion of particle-hole correlations around the DB mean field also can ensure thermodynamical consistency in the form of the Hugenholtz-van-Hove theorem [39,40].

In the present work we employ the results of two different DB calculations, those of ref. [24] and the more recent ones of ref. [26], denoted as DBHM and DBT, respectively, in the following. We will briefly characterise the difference between these two calculations. One difference is the use of different OBE potentials; in [24] a version of the Groningen potential and in [26] the Bonn A potential. In both cases the same set of six non-strange mesons with masses below 1 GeV is used and the fit to the NN phase shifts is of similar quality, however, the actual model parameters (coupling constants and form factors) are different. The main difference between these two approaches has a more complicated origin, which is discussed in detail in [25,26]. The DB structure equations (1)-(3) are matrix equations in spinor space. To determine the Dirac structure of the self-energy, *i.e.* the scalar ($\Sigma_{\rm s}$) and a vector (Σ_μ) contributions,

$$\Sigma_{\alpha\beta} = \mathbb{1}_{\alpha\beta}\Sigma_{\rm s} - \gamma^\mu_{\alpha\beta}\Sigma_\mu \,, \tag{4}$$

the $\mathcal{T}$-matrix has to be decomposed into its Lorentz components, *i.e.* scalar, vector, tensor, etc. contributions. This procedure is not free from ambiguities. Due to identical matrix elements for positive-energy states pseudo-scalar and pseudo-vector components cannot uniquely be disentangled for the on-shell $\mathcal{T}$-matrix. However, with a pseudo-scalar vertex, the pion couples maximally to negative-energy states which are not included in the standard Brueckner approach. This is inconsistent with the potentials used since the OBE potentials are based on the no-sea approximation. Hence, pseudo-scalar contributions due to the one-π exchange lead to large and spurious contributions from negative-energy states. In [25] it was shown that such spurious contributions dominate the momentum dependence of the nuclear self-energy, and, in particular, lead to an artificially strong momentum dependence inside the Fermi sea. It was further demonstrated in [25] that the method used in [24] fails to cure this problem and in [26] a new and reliable method was proposed to remove those spurious contributions from the $\mathcal{T}$-matrix.

Table 1. Saturation properties of nuclear matter, *i.e.* Fermi-momentum $k_{\rm F}$, saturation density $\rho_{\rm sat}$, binding energy per particle E/A, effective mass m^* and the compression modulus K in the DB calculations of [24] (DBHM) and [26] (DBT).

	$k_{\rm F}$ (fm^{-1})	$\rho_{\rm sat}$ (fm^{-3})	E/A (MeV)	m^* (MeV)	K (MeV)
DBHM	1.343	0.164	−13.6	558	250
DBT	1.39	0.185	−16.1	637	230

The saturation properties of the two DB calculations are given in table 1. It is seen there that the results of ter Haar and Malfliet (DBHM) [24] give a slightly better saturation density compared to [26] (DBT) but too little binding. DBT, in contrast, gives a good binding energy and also meets the empirical range of saturation. The stiffness of the EOS expressed by the compression moduli is similar for both approaches. A significant difference can be observed for the magnitude of the effective mass but both values are consistent with the knowledge from finite nuclei on the strength of the spin-orbit force (500 MeV $\leq m^* \leq$ 700 MeV) [20].

We also note that the relativistic effective mass, *i.e.* the Dirac mass $m^* = M - \Sigma_{\rm s}$ given in table 1, should be distinguished from the effective mass $m^*_{\rm NR}$ which in non-relativistic approaches is used to classify the non-locality of the mean field [12,13]. The latter is defined by

$$m^*_{\rm NR} = |\mathbf{k}| \left(\frac{\partial k^0}{\partial |\mathbf{k}|} \right)^{-1} \tag{5}$$

and is approximately $m^*_{\rm NR} \approx k^*_0 = \sqrt{\mathbf{k}^2 + m^{*2}}$. At ρ_0 the two models DBHM/DBT yield the following values $m^*_{\rm NR}(k_{\rm F})/M = 0.63/0.73$ which can be compared to the parameters used in refs. [12,13].

The corresponding equations of states are shown in fig. 1. Both models have a similar density dependence, however, due to the higher binding energy, DBT lies generally below DBHM. At high densities the softer character of DBT becomes a little more pronounced. For comparison also the widely used Skyrme parameterisations (soft/hard, denoted by SMD/HMD) with compression moduli of $K = 200/380$ MeV [4] are shown. It is seen that in particular DBT is close to the soft Skyrme parameterisation up to about $2\rho_0$ where it starts to become more repulsive.

Figure 2 shows the density dependence of the mean field. In the DBT approach the fields are generally smaller by about 50–100 MeV compared to DBHM. The same trend can be seen from fig. 3, where the momentum dependence of the scalar and vector potentials at densities $\rho_0 = 0.16$ fm^{-3}, $2\rho_0$ and $3\rho_0$ is shown. In both calculations scalar and vector fields decrease with increasing momentum in a similar way. Generally, the explicit momentum dependence is moderate at densities $\rho \leq \rho_0$ but becomes pronounced at higher densities. In ref. [24] constant values

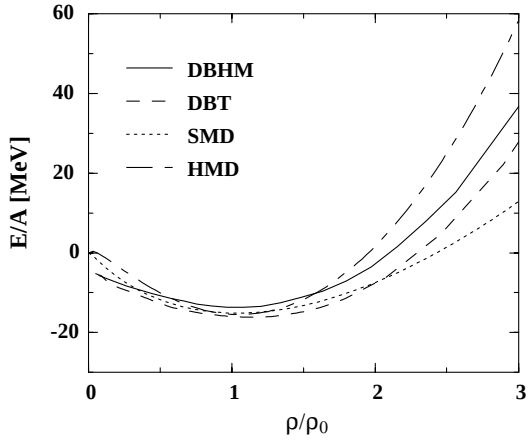

Fig. 1. Equation of states in the DB approaches. Solid line: DB calculations from [24], dashed line: DB calculations from [26]. For comparison also the soft/hard (SMD/HMD) momentum-dependent Skyrme parameterisations with a compression modulus of $K = 200/380$ MeV [4] are shown.

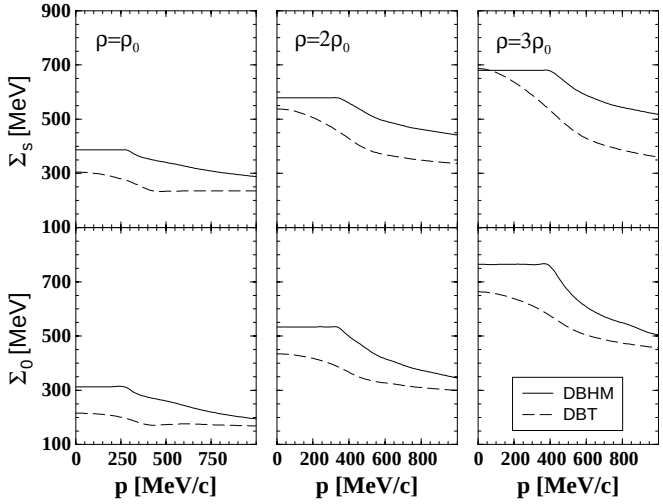

Fig. 3. Momentum dependence of the scalar (top) and vector (bottom) self-energies at $\rho = 1/2/3\rho_0$. The solid lines are DB calculations from [24] and the dashed curves from [26].

of Σ are taken for momenta below the Fermi momentum whereas the results of [26] reflect the full momentum dependence outside and inside the Fermi sea. The difference in the magnitude of the fields Σ_s and Σ_0 in the two approaches can be traced back to the different projection schemes discussed above. With the correct and complete pseudo-vector description for the pion contributions, the fields are dominated by the σ and ω contributions and the other mesons π(pseudo-vector coupling) ρ, η, δ give only small corrections [25,26].

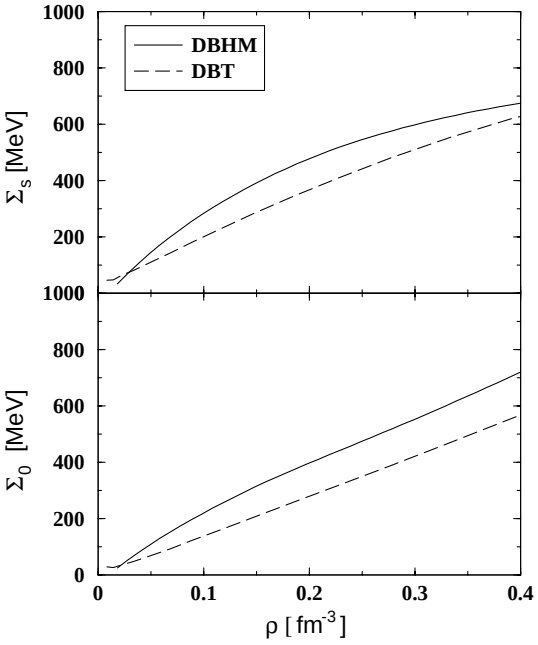

Fig. 2. Scalar (top) and vector (bottom) self-energies. The solid lines are DB calculations from [24], the dashed lines from [26].

Figure 4 shows the real part of the optical Schroedinger-equivalent nucleon potential, defined as

$$U_{\rm opt} = -\Sigma_{\rm s} + \frac{k^0}{M}\Sigma_0 + \frac{\Sigma_{\rm s}^2 - \Sigma_\mu^2}{2M} \ , \qquad (6)$$

in nuclear matter as a function of its laboratory energy $E_{\rm lab} = k^0 - M$. Note that the definition of an optical potential is not unique in the literature, *e.g.* in refs. [12,41] an optical potential is defined as the difference of the single-particle energies in the medium and in free space $U = k^0 - \sqrt{M^2 + \mathbf{k}^2}$. The optical potential defined by eq. (6) is the Schroedinger-equivalent relativistic potential [24] and can be covariantly defined by $U_{\rm opt} = (k_\mu^2 - M^2)/2M = ((k_\mu^* + \Sigma_\mu)^2 - M^2)/2M$ as a Lorentz scalar. Even a momentum-independent vector potential Σ_0 (as in the mean-field approximation of QHD) leads to a linear energy dependence of the optical potential (6), *i.e.* a momentum dependence $\frac{\Sigma_0(\rho)}{2M^2}p^2$. The explicit momentum dependence of the DB fields falls asymptotically as $\Sigma_{0,S} \sim (A + B/p)$ which still leads to a linear increase of $U_{\rm opt}$ at large energies. As seen in fig. 4 the DB model reproduces the empirical optical potential [3] extracted from proton-nucleus scattering for nuclear matter at ρ_0 reasonably well up to a laboratory energy of about 0.6–0.8 GeV. However, it is seen that the saturation behaviour at large momenta cannot be reproduced by DB calculations. In heavy-ion reactions at incident energies above 1 AGeV such a saturation behaviour is required to reproduce transverse flow observables [11]. Thus, DB mean fields start to become unrealistic around 1 AGeV. There exists presently no microscopic relativistic calculation which is able to reproduce this saturation behaviour of the optical potential. Therefore, we restrict our investigation of transverse flow observables to an energy range where the DB fields can be safely applied. At higher energies one has to rely on phenomenological approaches where the strength of the vector potential is artificially

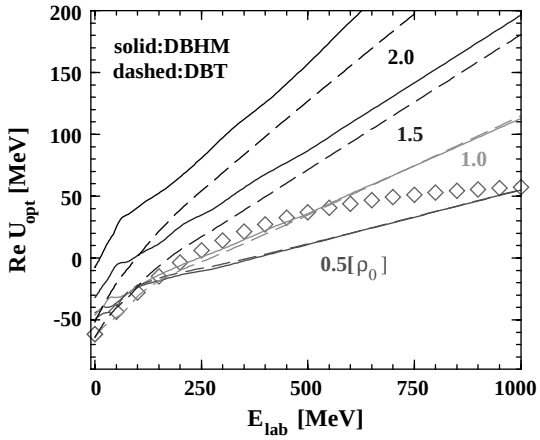

Fig. 4. Energy dependence of the optical potential. The solid lines are DB calculations from [24], the dashed lines from [26].

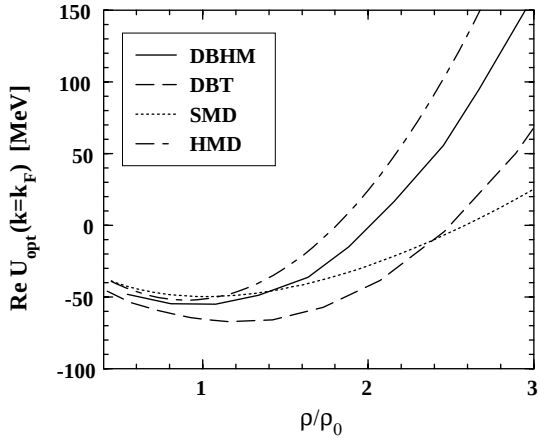

Fig. 5. Optical potential $U_{\rm opt}(\rho, k = k_{\rm F})$ at the Fermi surface as a function of density. Solid line: DB calculations from [24]; dashed line: DB calculations from [26]. For comparison also the soft/hard (SMD/HMD) momentum-dependent Skyrme parameterisations [4] are shown.

suppressed, *e.g.* by the introduction of additional form factors [11].

One should be aware that the empirical optical potential involves densities around ρ_0 and does not completely constrain the mean fields that enter in a heavy-ion collision, which involve large values of momentum and density. As a common feature, relativistic DB calculations show a strong and repulsive momentum dependence also at high densities [24,26,41] whereas, *e.g.* the non-relativistic $\mathcal{G}$-matrix [38] has a much less repulsive high-density behaviour. In first order, the strength of the repulsion in the relativistic case is determined by the magnitude of the vector field. As can be seen from fig. 4 the two approaches DBHM and DBT yield similar results at moderate densities $\rho \leq \rho_0$ but differences become substantial at high densities. The generally smaller fields of DBT result in a less repulsive potential at high densities. This behaviour becomes even more clear from fig. 5 where the optical potentials taken at the Fermi surface, *i.e.* at $k = k_{\rm F}$, are shown as a function of the density. For comparison also the potentials of the soft/hard momentum-dependent Skyrme parameterisations (SMD/HMD) [4] are given. For DBHM the interplay between density and momentum dependence of the optical potential is similar to the hard Skyrme force although the EOS is less repulsive at high densities. On the other hand, DBT is even more attractive than the soft Skyrme force at low densities and becomes more repulsive than the soft Skyrme force only above $2\rho_0$. Hence the character of the mean field obtained by the two DB model calculations show essential differences although the corresponding EOSs are similar. The test of DB fields in heavy-ion collisions where high densities ($\rho \approx 2$–$3\rho_0$) and momenta greater than the Fermi momentum can be reached, should allow to differentiate between the two models.

3 The CNM approximation

The DB approach discussed in the previous section describes equilibrated nuclear matter which is characterised by one Fermi sphere of a given Fermi momentum. In a local density approximation (LDA) these self-energies are directly inserted into the drift term of the RBUU equation. However, as discussed before, local momentum space anisotropies are a characteristic feature of energetic heavy-ion reactions. The time scales where such anisotropies occur are comparable with the compression phase of the process [15,32,33]. It was found that the local anisotropic momentum space can well be parametrised by two interpenetrating nuclear-matter currents, *i.e.* by two Fermi spheres in momentum space [32,33], or the Colliding Nuclear Matter (CNM) [34] which is schematically illustrated in fig. 6. The application of the relativistic DB model to CNM configurations has, however, not been realized yet, but only non-relativistic $\mathcal{G}$-matrix calculations have been performed for CNM [37].

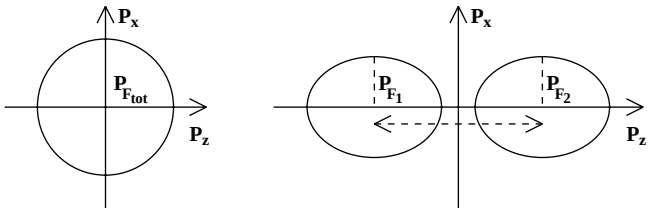

Fig. 6. Schematic representation of the LDA (nuclear matter) and LCA (colliding nuclear matter) approximations.

Therefore in ref. [34] a method was developed to extrapolate DB results to such CNM configurations. The CNM momentum distribution is constructed as a superposition of the single currents, *i.e.*

$$f_{12}(\mathbf{k}^*) = f_1(\mathbf{k}^*) + f_2(\mathbf{k}^*) + \delta f = \Theta(k_{\rm F_1} - k^*_\mu u^\mu_1) + \Theta(k_{\rm F_2} - k^*_\mu u^\mu_2) + \delta f\,, \quad (7)$$

where f_i are the covariant momentum space distributions of the two NM currents and $\delta f = -f_1 f_2$ is a correction term which takes into account Pauli-blocking effects in the overlap region of the two nuclear matter currents.

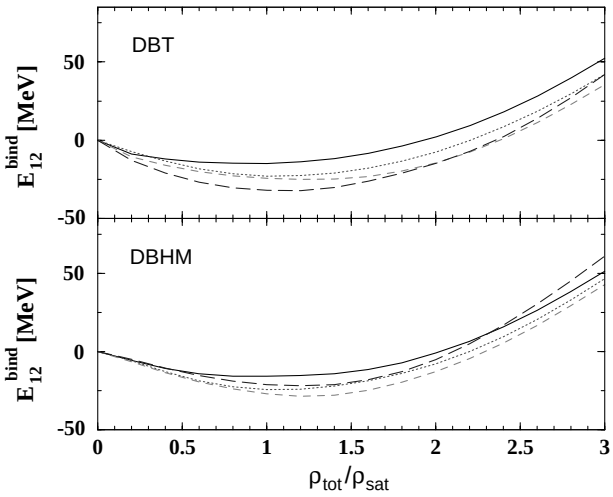

Fig. 7. Subtracted EOSs for the CNM approximation using the DB results of ref. [24] (top) and [26] (bottom). The different curves give the CNM EOSs for different relative velocities ($v_{\rm rel}$ = 0, 0.2, 0.4, 0.6 for solid, dotted, dashed and long-dashed curves, respectively).

The corresponding CNM self-energies $\Sigma_{\rm s,0}(k;\chi)$ depend explicitely on momentum and the configuration parameters $\chi \equiv \{k_{\rm F_1}, k_{\rm F_2}, v_{\rm rel}\}$ (Fermi momenta $k_{\rm F_{1,2}}$ and the relative velocity $v_{\rm rel}$). Averaging the CNM configuration, eq. (7), over momentum leads to mean self-energies which depend only on the parameters of the CNM momentum space distributions.

The consideration of anisotropy effects in the CNM approximation leads to non-equilibrium mean fields, which essentially differ from those of the equilibrium case. In analogy to the non-equilibrium self-energies we construct a non-equilibrium EOS [34], *i.e.* an equation of state which depends on the CNM parameters. In order to compare the compression energies it is useful to subtract the kinetic energy of the relative motion of the two nuclear-matter currents which yields the "subtracted" binding energy $E_{12}^{\rm bind}$ of the system. Figure 7 shows these EOSs for different symmetric ($k_{\rm F} \equiv k_{\rm F_1} = k_{\rm F_2}$) CNM configurations. It is seen in both models that the effective non-equilibrium EOS is softer compared to the equilibrium EOS (solid curves for vanishing relative velocity). However, the different density and momentum dependence of the two DB models leads to a different magnitude of this softening effect, in particular with increasing relative velocity.

This softening of the effective EOS in colliding nuclear matter can be understood by considering that, in the participant zone of the reaction, particles which belong to projectile and target are separated in momentum space. This geometrical effect works in a similar way as an additional degree of freedom and leads to a softening of the effective EOS experienced by the nucleons in such configurations. This type of phase space effect is not included in standard transport calculations for heavy-ion collisions, even when momentum-dependent interactions are used [12,13]. Phenomenological mean fields $U(\mathbf{x},\mathbf{k}) = U_{\rm loc}(\varrho(\mathbf{x})) + U_{\text{non-loc}}(\mathbf{x},\mathbf{k})$ are usually composed by a local, density-dependent potential $U_{\rm loc}(\varrho(\mathbf{x}))$ and a non-local momentum-dependent part $U_{\text{non-loc}}(\mathbf{x},\mathbf{k}) = \int \mathrm{d}^3k' f(\mathbf{x},\mathbf{k}') V(\mathbf{x},\mathbf{k}-\mathbf{k}')$ with V an effective momentum-dependent two-body interaction. Whereas $U_{\text{non-loc}}(\mathbf{x},\mathbf{k})$ accounts properly for the actual momentum space configurations $f(\mathbf{x},\mathbf{k}')$, the local part does not depend on the momentum space. Consequently, $U_{\rm loc}(\varrho)$ reflects a density dependence which is correct in equilibrated nuclear matter but does not apply to anisotropic momentum space configurations.

4 The transport model

In the present work heavy-ion collisions are treated by the relativistic (R)BUU equation [2,14,15]:

$$\left\{ k^*_\mu \partial^\mu_x + [k^*_\nu F^{\mu\nu} + m^*(\partial^\mu_x m^*)]\, \partial^{k^*}_\mu \right\} f(x,k^*) = I_{\rm coll}\,. \quad (8)$$

This equation describes the evolution of a classical one-body phase space distribution $f(x,k^*)$ under the influence of a self-consistent mean field, or the scalar and vector self-energies $\Sigma_{\rm s}$ and Σ^μ. The self-energies determine effective momenta and masses of the dressed quasi-particles in the nuclear medium $k^{*\mu} = k^\mu - \Sigma^\mu$, $m^* = M - \Sigma_{\rm s}$. The field strength tensor of the vector field $F^{\mu\nu} = \partial^\mu \Sigma^\nu - \partial^\nu \Sigma^\mu$ gives rise to a Lorentz force as in electrodynamics. This introduces in a most natural way a first-order momentum dependence which in non-relativistic treatments has to be parameterised explicitely [1,4,10]. The collision term describes 2-body collisions and is treated by cascade-like Monte Carlo simulations, as in relativistic versions of the QMD model [42]. We include the relevant nucleonic excitations at SIS energies, *i.e.* the $\Delta(1232)$ and $N^*(1440)$ resonances and their decay to one- and two-pion states. The cross-sections for elastic and inelastic scattering as well as differential cross-sections are taken from ref. [43] which are used also in QMD calculations at SIS energies [44,45]. The drift term of the RBUU equation (8) is numerically treated in the relativistic Landau-Vlasov method (RLV) [46]. This is a test particle method, where the test particles are represented by manifestly covariant Gaussians in phase space. In order to reduce numerical fluctuations a number of 50-100 test particles per nucleon was found to be sufficient here. The nuclei are initialised to fit density profiles obtained from self-consistent Thomas-Fermi calculations [46]. For both models (DBT and DBHM) we adjust the test particle distributions to the same reference distribution. The corresponding initialisations are stable over the durations of the considered reactions. Energy momentum conservation is fulfilled with an accuracy of 3–5% of the initial kinetic centre-of-mass energy of the colliding nuclei.

The anisotropic phase space effects discussed above are incorporated in heavy-ion collisions by applying the CNM or non-equilibrium DB mean fields in the framework of a Local Configuration Approximation (LCA) [14,15,33]. In this approach the phase space is parametrised locally by a CNM configuration where the invariant configuration

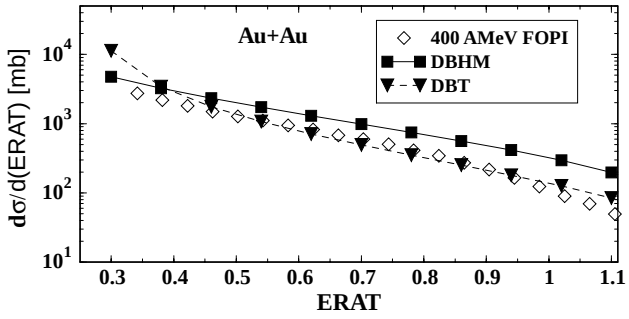

Fig. 8. ERAT cross-sections for protons in Au + Au reactions at 0.4 AGeV beam energy. Transport calculations with the DB mean fields from ref. [24] (DBHM) [26] (DBT) are compared with the FOPI data [47].

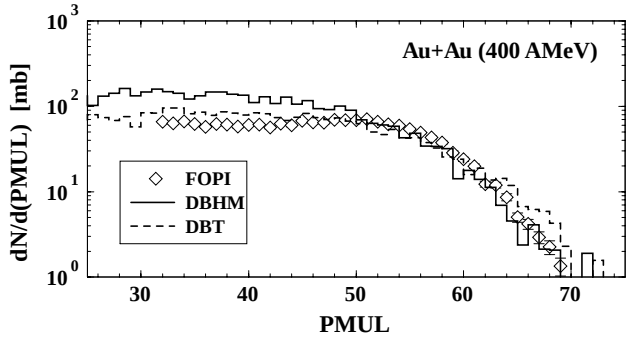

Fig. 9. Multiplicity of charged particles. Solid line: DB calculations from [24]; dashed line: DB calculations from [26].

parameters χ are directly determined from the phase space distribution $f(x, k^*)$. Transport calculations have shown that the collective flow is reduced if the non-equilibrium effects are taken into account [15] which is consistent with a softening of the effective EOS in heavy-ion collisions as discussed above.

5 Collective flow effects

In this section different types of collective flow observables are investigated in transport calculations using the DBHM/DBT mean fields in the local phase space configuration approximation (LCA). To compare with experiments, the same methods are used for centrality selection and reaction plane determination, and the theoretical results are subjected to filter routines to simulate the experimental detector efficiencies, if necessary. Since we mainly compare to results from the FOPI Collaboration [6,31,47, 48] these correspond to the FOPI (Phase-I or Phase-II) set up. These filters are sensitive to fragment distributions. Thus we also generate fragments in the final state of the reaction (at $\approx$ 100–200 fm/c depending on the incident energy) using a phenomenological phase space coalescence model. The coalescence parameters in coordinate and momentum space are separately adjusted for both models DBT and DBHM to fit the experimental mass distributions of light fragments ($Z \leq 3$) [15,49]. After the cluster formation we apply the same procedure for the reaction plane reconstruction as the FOPI group. The corresponding corrections are very close to those obtained with the IQMD model [50].

Criteria for the determination of the centrality class of an event are the multiplicity of charged particles (PMUL) and/or the ratio of transversal to longitudinal energy (ERAT) [51]. As an example, in figs. 8 and 9 these observables are shown for protons at an energy of 0.4 AGeV and compared to FOPI data [47,51]. Figure 8 displays the differential cross-section dσ/d(ERAT). Large ERAT values correspond to central reactions whereas small values indicate semi-peripheral and peripheral reactions [15,47, 51]. A qualitative agreement with experiment is achieved for both mean fields, with DBHM somewhat overestimating the data. At small ERAT values below about 0.2 the quantity dσ/d(ERAT) is strongly affected by trigger effects and drops very rapidly. As discussed in [47] model calculations tend to strongly overestimate the data below 0.3, which is due to detector cuts which remove the projectile remnant. Since such remnants, *i.e.* very heavy clusters, are not formed in transport calculations the cross-section is overpredicted in very peripheral collisions although the total reaction cross-section coincides with the experimental one.

In fig. 9 the multiplicity distributions dσ/d(PMUL) are shown. Also here the agreement with experiment is reasonable for DBHM and quite good for DBT. Particularly, we can reproduce the plateau (in logarithmic scale) of these distributions which is used in the centrality selection. Altogether, the good agreement with experiment makes the centrality selection reliable using either the PMUL or ERAT observable. In the following we will mainly use the PMUL criterion. The correlation between multiplicity and centrality intervals is defined as in experiments in the following way: the lower limit of the highest multiplicity bin, called PM5, is fixed at half of the plateau value, and the remaining multiplicity range is divided into four equally spaced intervals, denoted by PM4 to PM1. PM5 then corresponds to most central reactions, and PM4 and PM3 to semi-central and peripheral ones, respectively [51].

5.1 Nuclear stopping

We start the flow analysis with the longitudinal distributions which are characterised in terms of the rapidity $Y_{\rm cm} = \frac{1}{2}\ln(1+\beta_{\rm cm})/(1-\beta_{\rm cm})$. Here the normalised rapidity $Y^{(0)} = Y_{\rm cm}/Y_{\rm cm}^{\rm proj}$ is considered.

The rapidity distributions are shown in fig. 10 for different centrality classes (using the ERAT selection [47]). This observable is strongly affected by detector cuts [47, 51], which is reflected in the asymmetry of these distributions relative to the cm-rapidity, due to the angular limitations of the FOPI detector (Phase-I) [51].

It is seen that both models are able to generally reproduce the experimental results. Stopping is influenced most strongly by the choice of the NN cross-sections, which are

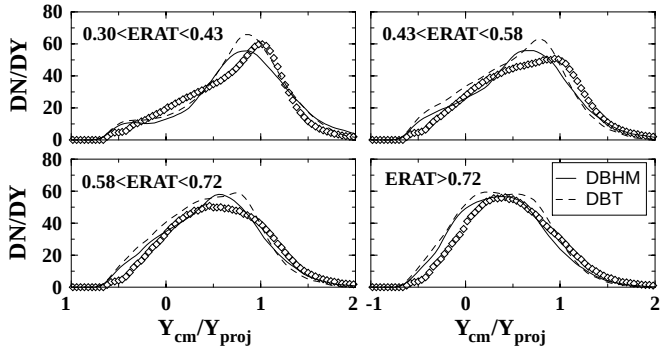

Fig. 10. Rapidity distributions for Au + Au collisions at 0.4 AGeV beam energy. The different centrality intervals run from peripheral (upper left) to central (lower right) collisions. The solid lines are DB calculations from [24], the dashed lines from [26].

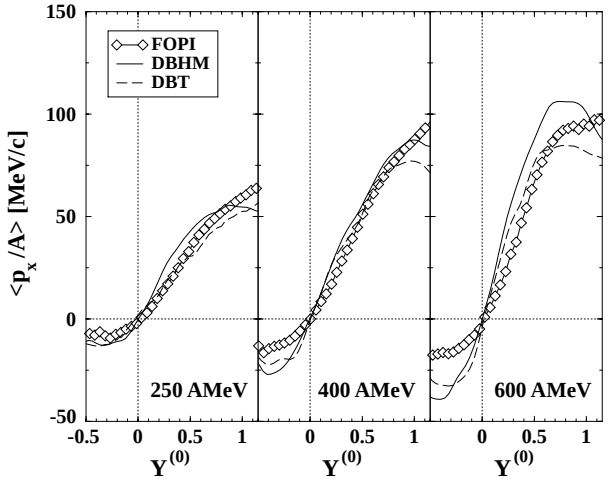

Fig. 11. Mean in-plane transverse flow of protons *versus* normalised rapidity for semi-central (PM4) Au + Au collisions at 0.25, 0.4 and 0.6 AGeV beam energy. The solid lines are DB calculations from [24], the dashed lines from [26]. The experimental results are taken from [52].

the same in both models. An indirect influence also from the EOS can be expected since a softer and less repulsive EOS leads to more compression and thus to more collisions. However, the differences are not very pronounced which reflects the fact that the EOSs are still similar in the explored density regime and do not differ too much even at the maximal densities reach in central reactions ($\rho \approx 2$–$3\ \rho_0$). In peripheral collisions, where the deflection of spectator matter by the repulsive momentum-dependent component of the mean field plays a more dominant role, the rapidity distributions show bigger differences. Similar trends have been observed in in ref. [47] with soft/hard Skyrme forces.

5.2 In-plane flow

Next we consider the emission of matter projected onto the reaction plane described by the mean in-plane or sideward flow [5,6]. Figure 11 compares the mean in-plane proton flow $\langle p_x/A \rangle$ in semi-central (PM4) Au + Au collisions at incident energies of 0.25, 0.4 and 0.6 AGeV to the FOPI data from [52]. Both models reproduce the energy-dependent increase of the proton flow and are generally in good agreement with the data. We observe that DBHM leads to a stronger in-plane flow in the spectator rapidity region whereas the slope near midrapidity $Y^{(0)} \sim 0$ is less affected by the differences in density and momentum dependence of the mean fields. At 0.6 AGeV DBHM starts to overpredict the slope of the in-plane flow, whereas DBT is still in reasonable agreement with experiment. This reflects again the more repulsive character of the DBHM forces which becomes more pronounced with increasing energy, in particular in the spectator region $Y^{(0)} \sim 1$. On the other hand, DBT describes the in-plane flow well around midrapidity but slightly under predicts it in the spectator region.

The situation is more clearly seen when the mean directed flow $P_x^{\rm dir}$, *i.e.* the in-plane flow integrated over the forward hemisphere ($Y^{(0)} \geq 0$), is considered. In fig. 12 the excitation function of $P_x^{\rm dir}$ is compared to the FOPI data [52], again for PM4. $P_x^{\rm dir}$ is a measure for the overall repulsion experienced by the reaction. The comparison with data shows that both microscopic models can explain the experimental results relatively well. However, above 0.4 AGeV the experimental excitation function of $P_x^{\rm dir}$ shows a saturation behaviour which is not completely reproduced. Here, as already seen in fig. 11, DBT is in good agreement with experiment at higher energies but underpredicts the flow at lower energies. For DBHM the situation is just opposite. Due to the FOPI acceptance $P_x^{\rm dir}$ is dominated by the bounce-off of spectator matter at $Y^{(0)} \sim 1$ (see the corresponding rapidity distributions in fig. 10) which explains the low value of DBT at 0.4 AGeV. The more repulsive character of the DBHM mean fields, in particular at high densities, produces a bounce-off of the spectator remnants in the reaction plane, resulting in too high transverse momenta near spectator rapidities at energies above 0.6 AGeV. Since the maximal densities reached in the model calculations are changing very little between 0.4 and 0.8 GeV the slope of the $P_x^{\rm dir}$ excitation function is determined mostly by the momentum dependence of the mean field and less by the density dependence of the EOS. This may be considered as a way to test the average momentum dependence of the models. However, as discussed below an integrated observable reflects the average dynamics which is dominated by densities around ρ_0. To extract more decisive information on the momentum dependence at supranormal densities, differential observables should be considered.

As a differential observable the dependence of the in-plane flow on transverse momentum $p_{\rm t}$ has recently attracted great interest. While the global behavior of the transverse flow, as expressed by $P_x^{\rm dir}$ or $\langle p_x/A \rangle$, gives an average over the entire evolution of the collision, the $p_{\rm t}$-dependence allows to obtain information on different stages of the reaction. High $p_{\rm t}$ nucleons, but also pi-

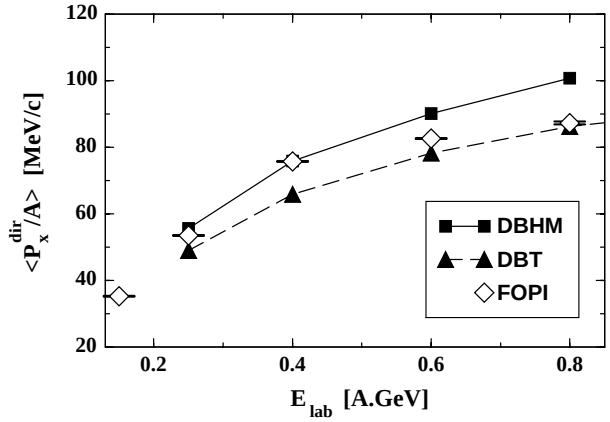

Fig. 12. Excitation function of the mean directed in-plane flow for semi-central (PM4) Au + Au collisions (data from [52]). Solid line: DB calculations from [24]; dashed line: DB calculations from [26].

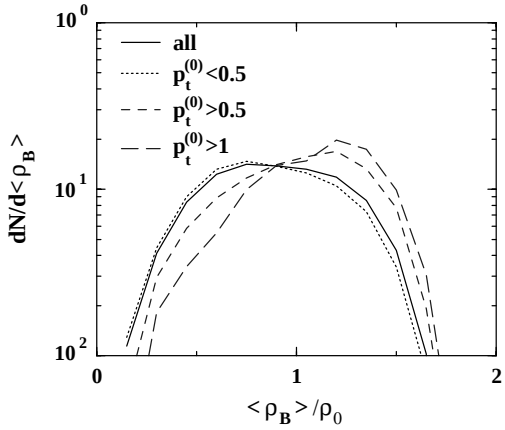

Fig. 13. The density distribution which is correlated with the dynamical history of the particles is shown for different $p_{\rm t}^{(0)}$ cuts for a semi-central ($b = 6$ fm) Au + Au collisions at 0.4 AGeV.

ons [45], originate from the early and high density phase of the reaction. This is a general feature of heavy-ion collisions and seems to hold at bombarding energy from SIS [13] to AGS and SPS energies [53]. In ref. [12] it was pointed out that the $p_{\rm t}$-dependence of the transverse flow in peripheral reactions is particularly sensitive to the momentum dependence of the nuclear mean field at supranormal densities. Consistent with this observation, in [13] it was demonstrated that the emission time of high $p_{\rm t}$ particles at midrapidity coincides well with the high density phase of the reactions. To be more quantitative, in fig. 13 we consider the correlation between the averaged density $\langle\rho_B\rangle$ at which the particles are emitted and the transverse momentum $p_{\rm t}$. Exemplarily a semi-peripheral ($b = 6$ fm) Au + Au reaction at 0.4 AGeV is considered. Since particles interact with the surrounding matter over the entire duration of the reaction more or less strongly —with the mean field and by binary collisions— it is *a priori* not clear how to define an emission time and, correspondingly, a density from which the particles carry information. It is, however, natural to select that time and that corresponding density where the particles experience their most violent changes in momentum. This can be done by the following quantity:

$$\langle\rho_B\rangle = \sum_i \int {\rm d}t \rho_B(\mathbf{x}_i, t) \frac{|\dot{\mathbf{p}}_i|}{|\mathbf{p}_i|} \;\; / \;\; \sum_i \int {\rm d}t \frac{|\dot{\mathbf{p}}_i|}{|\mathbf{p}_i|} \;\; , \qquad (9)$$

where the index i runs over all baryons. Equation (9) samples over the densities weighted by the relative changes of the momenta. This is a generalisation of the "freeze-out" density because it takes the whole reaction history into account. Since experimentally only the final-state momenta are detected, this quantity is useful to establish a correlation between final observables and the stages of the reaction on which the particles carry information. The resulting emission densities are generally moderate because one averages over the entire phase space, *i.e.* over participant and spectator regions, and over the complete reaction history including the dilute expansion phase. Applying different $p_{\rm t}$-cuts ($p_{\rm t}^{(0)} = p_{\rm t}/p_{\rm cm}^{\rm proj}$) one sees that the low $p_{\rm t}$-particles and hence the bulk of the nucleons experiences a dynamical evolution which takes mainly place at densities below saturation density when integrated over the complete space-time of the reaction. The high $p_{\rm t}$-particles ($p_{\rm t}^{(0)} > 0,5$), in contrast, are governed by larger densities. As a consequence, they probe the momentum dependence of the optical potential at supranormal densities. In fig. 13 as in the calcualtions below (fig. 14) we considered projectile rapidities, but the observed behaviour is even more pronounced in the midrapidity region.

The flow and its $p_{\rm t}^{(0)}$-dependence has been discussed in terms of a Fourier analysis of the experimental azimuthal distribution [54]

$$\frac{{\rm d}N}{{\rm d}\phi}(p_{\rm t}^{(0)}, Y^{(0)}) = v_0(1 + 2v_1\cos(\phi) + 2v_2\cos(2\phi)) \,. \quad (10)$$

In eq. (10) v_0 is a normalisation constant, $v_1(p_{\rm t}^{(0)},\ Y^{(0)})$ describes the in-plane collective flow and $v_2(p_{\rm t}^{(0)},\ Y^{(0)})$ the emission perpendicular to the reaction plane, also called elliptic flow. The quantities $v_{1,2}$ can be determined directly as $v_1 = \langle p_x/p_{\rm t}\rangle$ and $v_2 = \langle (p_x^2 - p_y^2)/p_{\rm t}^2\rangle$, where $p_{\rm t} = \sqrt{p_x^2 + p_y^2}$ is the transverse momentum per nucleon.

Figure 14 shows the $p_{\rm t}^{(0)}$-dependence of the in-plane flow (v_1) at normalised rapidities $0.5 \le Y^{(0)} \le 0.7$ for semi-central (PM4) Au + Au reactions at 0.4 AGeV incident energy for protons ($Z = 1$) and for light fragments ($Z = 2 + 3$).

A significant dependence of the differential in-plane flow on the DB model is observed. At low transverse momenta ($p_{\rm t}^{(0)} \le 0.2$) the two models do not show large differences. Since the mean transverse flow is dominated by low $p_{\rm t}$-particles the $\langle p_x/A\rangle$ observable therefore does not differentiate very much between the two models in the present situation. Consequently, in fig. 11 the two curves for $\langle p_x/A\rangle$ (0.4 AGeV) are very similar to each other in

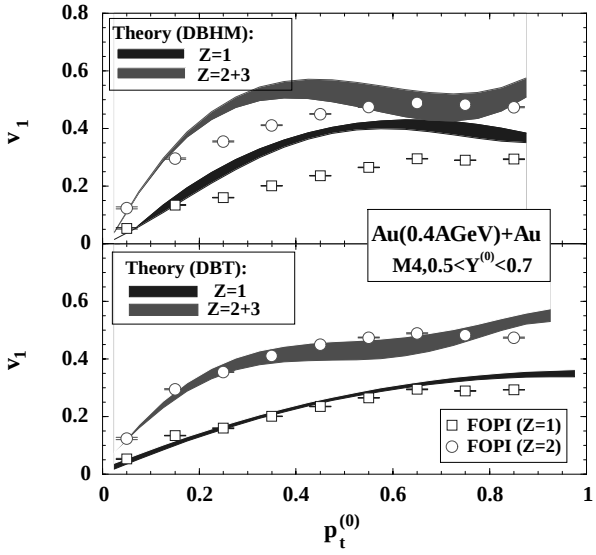

Fig. 14. In-plane flow in terms of the first Fourier coefficient (see eq. (10)) for semi-central (PM4) Au + Au collisions at 0.4 AGeV for protons and light fragments (data are from [55]). Statistical uncertainties of the calculations are indicated by bands.

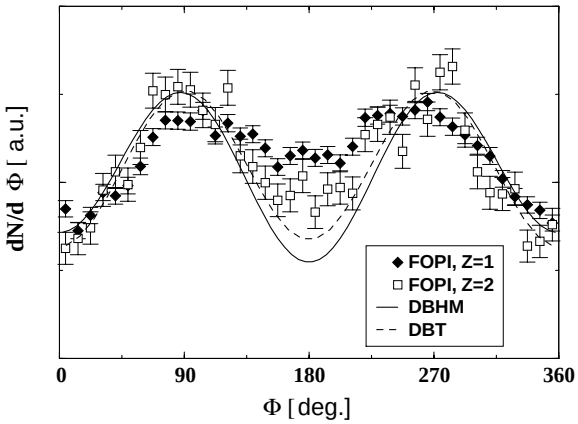

Fig. 15. Azimuthal distributions at midrapidity ($|\Delta Y^{(0)}| \leq 0.15$) for semi-central Au + Au collisions at 0.6 AGeV beam energy (data from [50]).

the considered rapidity range. However, the difference between the models becomes more pronounced when higher transverse momenta ($p_t^{(0)} \geq 0.2$) are studied. In fig. 14 DBT reproduces the data very well for both, protons and light fragments, whereas DBHM overpredicts the flow significantly which reflects its more repulsive character at baryon densities above ρ_0. The comparison to data favours a weaker repulsion at higher densities as predicted by DBT. In contrast to the global $P_x^{\rm dir}$ observable the quantity $v_1(p_t^{(0)}, Y^{(0)})$ is more sensitive to high density matter in the participant region.

The situation is similar for light fragments ($Z = 2+3$) which, however, show a stronger collectivity compared to free nucleons, as also seen by the higher value of v_2 in fig. 14. This can be understood by assuming that heavier fragments are mainly formed in the spectator regions, whereas the free nucleons originate from the entire phase space. Thus, one obtains on the average a higher mean transverse momentum $\langle p_x/A \rangle$ for fragments than for nucleons. This scenario of the fragment formation is consistent with the findings in ref. [49] that the spectator enters into an instability region with conditions which are near the experimental ones for a liquid-gas phase transition [56].

5.3 Out-of-plane flows

A preferential out-of-plane emission of particles, the so-called squeeze-out, is characterised by negative values of the second Fourier coefficient v_2 in eq. (10), whereas a positive value of v_2 indicates in-plane flow [54]. A related variable to characterise the azimuthal anisotropy of particle emission is the squeeze-out ratio R_N defined by [57]

$$R_N = (N(\Phi = 90^\circ) + N(\Phi = 270^\circ))/(N(\Phi = 0^\circ) + N(\Phi = 180^\circ)) = (1 - 2v_2)/(1 + 2v_2) \quad . \qquad (11)$$

In terms of R_N an isotropic emission corresponds to $R_N = 1$, $R_N > 1$ indicates squeeze-out and $R_N < 1$ a preferential in-plane emission. At lower energies squeeze-out is mainly due to shadowing of the participant particles by the spectators and it is therefore most pronounced for midrapidity particles. A sensitive way to probe the momentum dependence of the mean field is the transverse momentum dependence of the elliptic flow v_2. In contrast to central reactions where the squeeze-out is influenced by both, the static and the momentum-dependent part of the mean field, peripheral reactions allow to decouple the momentum dependence to some extent from the static part. In ref. [12] this has been demonstrated for v_2 at high p_t in peripheral reactions and was also confirmed by the investigations of [13]. Since high p_t-particles almost exclusively stem from the high density phase they probe the momentum dependence of the optical potential at supranormal densities, as was seen also in fig. 13.

First in fig. 15 we consider semi-central (PM4) reactions. It shows the azimuthal distributions at midrapidity for all charged particles (nucleons plus fragments) in Au + Au at 0.6 AGeV. The calculations are compared to experimental results from FOPI [50] for $Z = 1$ and $Z = 2$ fragments. The data show a stronger out-of-plane emission for $Z = 2$ fragments relative to those for nucleons which is due to to the higher collectivity of fragments as discussed above. Due to limited statistics, the theoretical values in fig. 15 are given for all charged particles. We observe a qualitatively good agreement between theory and experiments, although both calculations slightly overestimate the experimental squeeze-out signal.

Figure 16 shows the p_t-dependence of the elliptic flow v_2 in peripheral Au + Au collisions (PM3 multiplicity interval, $b_{\rm mean} \sim 7$ fm) at 0.4 AGeV. Consistent with the picture that squeeze-out is mainly due to shadowing, which is most effective in the early high density phase of

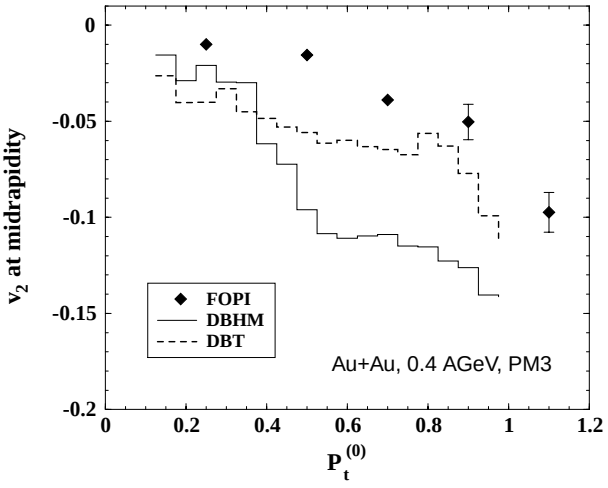

Fig. 16. Transverse momentum dependence of the elliptic flow at midrapidity ($|\Delta Y^{(0)}| \leq 0.1$) v_2 for peripheral (PM3) Au + Au collisions at 0.4 AGeV. Data are taken from [48].

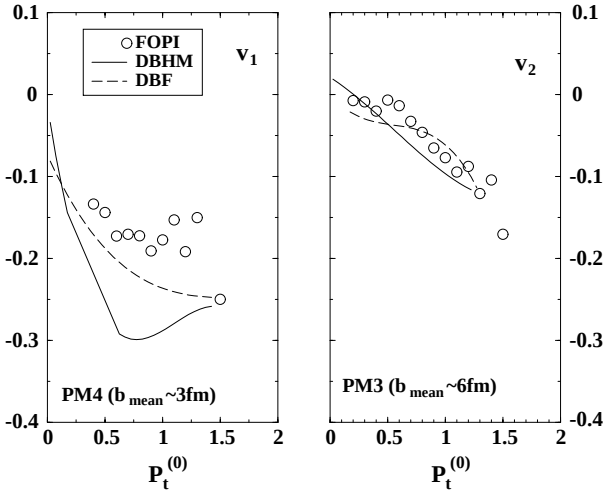

Fig. 17. Transverse momentum dependence of the first (v_1, left) and second (v_2, right) azimuthal flow Fourier coefficients for the system Ru + Ru at 0.4 AGeV incident energy extracted in rapidity intervals of $-0.7 < Y^{(0)} < -0.5$ (left) and $-0.3 < Y^{(0)} < -0.1$ (right) for semi-central (PM4) and peripheral (PM3) reactions, respectively (data from [31]).

the reaction, the elliptic flow becomes increasingly negative with increasing p_t. A physical explanation for this behaviour is that a strong repulsive momentum-dependent component of the nuclear interaction deflects these particles from the central zone more violently. This leads to enhanced shadowing by the spectator remnants inside the reaction plane and a stronger emission out-of-plane. This effect is clearly seen for the two types of interactions used here: Due to the stronger repulsive momentum dependence of the DBHM forces at supranormal densities the squeeze-out signal increases much stronger with p_t than for DBT, which on the other hand, is closer to the data of [48].

This behaviour is also consistent with the findings of ref. [48] where soft and hard Skyrme forces within the framework of the QMD model were subjected to a comparison of the same observable. The softer equations of state (soft Skyrme in [48] and DBT in the present case) yield a slower increase of v_2 and are in reasonable agreement with experiment. However, in ref. [48] both version of Skyrme forces have an identical momentum dependence whereas in the present case DBHM is significantly more repulsive at large densities. In the analysis of ref. [13], on the other hand, parameterisations were used which show the same density dependence, *i.e.* the same EOS, but differed in their momentum dependence. A stronger repulsive character of the model, expressed by both, a stiffer EOS and/or a stronger momentum dependence generally results in a stronger squeeze-out signal for high p_t-particles. The authors of ref. [13] favour a parameterisation (HM in ref. [13]) which yields results for this observable close to DBHM in our case. The comparison to the data of [48] in fig. 16 supports, however, a weaker momentum dependence at supranormal densities.

In fig. 17 the same analysis is performed for the Ru + Ru system. Here the differential components of the in-plane and out-of plane flow in terms of the Fourier coefficients v_1 and v_2 as a function of the transverse momentum and rapidity are shown. The rapidity intervals are $-0.7 < Y^{(0)} < -0.5$ and $-0.3 < Y^{(0)} < -0.1$ for the v_1 and v_2 analysis, respectively. Both, DBHM and DBT are in fair agreement with the FOPI data [31] on the v_2 observable. However, the p_t-dependence of the in-plane flow v_1 strongly depends on the model. As already observed for the Au + Au system (fig. 14) DBHM strongly overpredicts the flow v_1 at intermediate p_t. Thus, we conclude that the differences observed in the v_1 observable are due to the different momentum dependence of the fields. The v_2 observable shows here much less model dependence than, *e.g.*, in the Au + Au system. In the smaller system the compressional effects are smaller which reduces the sensitivity to the different momentum dependence.

In fig. 18 the centrality dependence of the squeeze-out ratio R_N at midrapidity ($|\Delta Y^{(0)}| < 0.15$) for particles with high transverse momenta ($0.4 < p_t^{(0)} < 0.55$) is shown. The decrease of the squeeze-out ratio R_N at higher impact parameters can be explained by the strong vector repulsion of the nuclear mean field. Again both models can reproduce the centrality dependence of the experimental data qualitatively, but not in detail. The DBHM calculations overpredict the data at low impact parameters, whereas DBT underpredicts the data for peripheral collisions. Similar results have been found in recent studies of the FOPI Collaboration in comparison with the IQMD model with soft/hard Skyrme forces [31]. Finally, fig. 19 shows the excitation function of the total elliptic flow v_2 at midrapidity. With increasing beam energy the emission is preferentially perpendicular to the reaction plane ($v_2 < 0$) which approaches a maximum around 0.4 AGeV and then decreases again. This behaviour can be understood by shadowing and compression effects as discussed in detail in ref. [58]. Again both models reproduce the general trend of a sample of experimental data from FOPI [48], EOS [58],

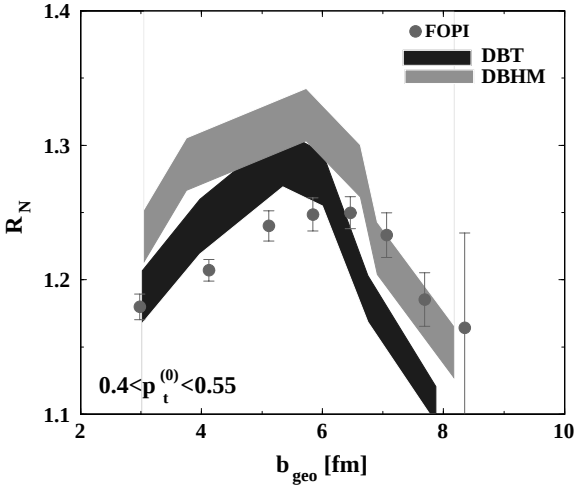

Fig. 18. Centrality dependence of the squeeze-out ratio R_N at midrapidity ($|\Delta Y^{(0)}| < 0.15$) for Au + Au collisions at 0.4 AGeV (data from [50]). Statistical errors of the calculations are indicated by bands.

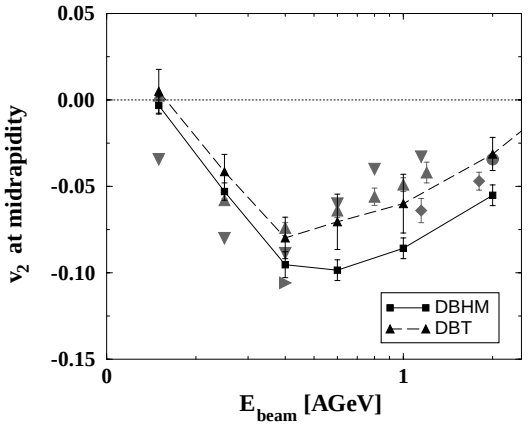

Fig. 19. Energy dependence of the elliptic flow v_2 at midrapidity. The data are taken from the FOPI (triangles) [48], EOS (diamonds) [58], Plastic Ball (down triangles) [6], LAND (right triangle) [6] and E895 (circle) [58].

Plastic Ball [6], LAND [6] and E895 [58] shown in fig. 19. However, with DBHM the maximum of negative v_2 values is slightly shifted to higher energies and the absolute values are larger. The experimental data show strong variations in the magnitude of the v_2 coefficient which cover the range of the theoretical calculations. However, DBT better reproduces the maximum at the correct energy and lies closer in absolute magnitude to the most recent data from FOPI [48]. Assuming that the latter are the most reliable measurements, *e.g.* with respect to reaction plane corrections etc., the comparison to experiment favours the DBT mean fields.

6 Summary

We investigated the collective nucleon flow in heavy-ion collisions at intermediate energies (0.15–1 AGeV) within a relativistic BUU transport model with mean fields based on relativistic Dirac-Brueckner-Hartree-Fock (DB) calculations for nuclear matter. The anisotropy of the local momentum space in the participant region of heavy-ion reactions was taken into account in the colliding nuclear matter approximation.

We compared two different DB fields, those of ter Haar and Malfliet (DBHM) and the more recent calculations performed by the Tübingen group (DBT). From a theoretical point of view the latter ones have a stronger physical foundation since spurious contributions from a strong coupling of a pseudo-scalar πNN vertex to negative-energy states were removed by an improved projection scheme for the in-medium T-matrix. The DBT model EOS is slightly softer ($K = 250/230$ MeV for DBHM/DBT) and the effective mass is significantly larger ($m^* = 558/637$ MeV for DBHM/DBT) than for the DBHM model. This results in smaller fields and a less repulsive optical potential for DBT. The smaller repulsion of the DBT model is also expressed in a terms of a larger non-local effective mass ($m^*_{\rm NR} = 0.63/0.73\ M$ for DBHM/DBT) which is commonly used in non-relativistic approaches in order to classify the strength of the momentum dependence of the potential.

Both models yield a reasonable description of in-plane and out-of-plane flow observables. A more detailed comparison to data, in particular the transverse momentum dependence of v_1 and v_2 favours the softer EOS and the less repulsive character of the DBT optical potential at supranormal densities. This observation is consistent with the information obtained from subthreshold K^+ production where also the scenario of a soft EOS is supported [59, 36]. At 0.6 and 0.8 AGeV DBT also yields a very accurate description of the transverse in-plane flow whereas at lower energies the in-plane flow requires some more repulsion as provided by the DBHM model. Interestingly, a similar observation was made in the non-relativistic approach of ref. [13].

In summary, the microscopic DB approach, where no parameters are adjusted to the nuclear-matter saturation properties nor to the empirical optical nucleon-nucleus potential, predicts a density and momentum dependence of the mean field which to a large extent is consistent with the observations from heavy-ion collisions.

We are grateful to A. Andronic from FOPI for many discussions concerning the interpretation of data.

References

1. E.A. Uehling, G.E. Uhlenbeck, Phys. Rev. **43**, 552 (1933); P. Danielewicz, Ann. Phys. (N.Y.) **152**, 239 (1984); G.F. Bertsch, S. Das Gupta, Phys. Rep. **160**, 189 (1988).
2. B. Blättel, V. Koch, U. Mosel, Rep. Prog. Phys. **56**, 1 (1993).
3. S. Hama, B.C. Clark, E.D. Cooper, H.S. Sherif, R.L. Mercer, Phys, Rev. C **41**, 2737 (1990); E.D. Cooper, S. Hama, B.C. Clark, R.L. Mercer, Phys. Rev. C **47**, 297 (1993).
4. J. Aichelin, H. Stöcker, Phys. Lett. B **176**, 14 (1986).

5. W. Reisdorf, H.G. Ritter, Annu. Rev. Nucl. Part. Sci. **47**, 663 (1997).
6. N. Herrmann, J.P. Wessels, T. Wienold, Annu. Rev. Nucl. Part. Sci. **49**, 581 (1999) and references therein.
7. T. Maruyama, W. Cassing, U. Mosel, S. Teis, K. Weber, Nucl. Phys. A **573**, 653 (1994).
8. Y.M. Zheng, C.M. Ko, Bao-An Li, Bin Zhang, Phys. Rev. Lett. A **83**, 2534 (1999).
9. J. Nemeth, G. Papp, H. Feldmeier, Nucl. Phys. A **647**, 107 (1999).
10. P.K. Sahu, A. Hombach, W. Cassing, M. Effenberger, U. Mosel, Nucl. Phys. A **640**, 493 (1998); A. Hombach, W. Cassing, S. Teis, U. Mosel, Eur. Phys. J. A **5**, 157 (1999).
11. P.K. Sahu, W. Cassing, U. Mosel, A. Ohnishi, Nucl. Phys. A **672**, 376 (2000).
12. P. Danielewicz, Nucl. Phys. A **673**, 375 (2000).
13. A.B. Larionov, W. Cassing, C. Greiner, U. Mosel, Phys. Rev. C **62**, 064611 (2000).
14. C. Fuchs, T. Gaitanos, H.H. Wolter, Phys. Lett. B **381**, 23 (1996).
15. T. Gaitanos, C. Fuchs, H.H. Wolter, Nucl. Phys. A **650**, 97 (1999).
16. B.D. Serot, J.D. Walecka, *Advances in Nuclear Physics*, Vol. **16**, edited by J.W. Negele, E. Vogt (Plenum Press, New York, 1986) p. 1.
17. P. Ring, Prog. Part. Nucl. Phys. **78**, 193 (1996).
18. F. Weber, J. Phys. G **25** (1999) R195.
19. B.D. Serot, J.D. Walecka, Int. J. Mod. Phys. E **6**, 515 (1997).
20. R.J. Furnstahl, B.D. Serot, H.-B. Tang, Nucl. Phys. A **615**, 441 (1997); H.W. Hammer, R.J. Furnstahl, Nucl. Phys. A **678**, 272 (2000).
21. M. Lutz, B. Friman, Ch. Appel, Phys. Lett. B **474**, 7 (2000).
22. G.J. Horowitz, B.D. Serot, Phys. Lett. B **137**, 287 (1984); Nucl. Phys. A **464**, 613 (1987).
23. W. Botermans, R. Malfliet, Phys. Rep. **198**, 115 (1990).
24. B. ter Haar, R. Malfliet, Phys. Rep. **149**, 207 (1987).
25. C. Fuchs, T. Waindzoch, A. Faessler, D.S. Kosov, Phys. Rev. C **58**, 2022 (1998).
26. T. Gross-Boelting, C. Fuchs, A. Faessler, Nucl. Phys. A **648**, 105 (1999).
27. C. Fuchs, H. Lenske, H.H. Wolter, Phys. Rev. C **52**, 3043 (1995).
28. R. Machleidt, *The Meson Theories of Nuclear Forces and Nuclear Structure*, Adv. Nucl. Phys. **19**, 189 (1989).
29. R. Machleidt, nucl-th/9911059.
30. C. Fuchs, E. Lehmann, L. Sehn, F. Scholz, J. Zipprich, T. Kubo, Amand Faessler, Nucl. Phys. A **603**, 471 (1996).
31. FOPI Collaboration (N. Bastid), *Proceedings to Structure of the Nucleus at the Dawn of the Century* (Publisher, Bologna, 2000).
32. C. Fuchs, P. Essler, T. Gaitanos, H.H. Wolter, Nucl. Phys. A **626**, 987 (1997).
33. R.K. Puri, N. Ohtsuka, E. Lehmann, A. Faessler, H.M. Martin, D.T. Khoa, G. Batko, S.W. Huang, Nucl. Phys. A **536**, 201 (1992).
34. L. Sehn, H.H. Wolter, Nucl. Phys. A **601**, 473 (1996).
35. D.T. Khoa, N. Ohtsuka, M.A. Matin, A. Faessler, S.W. Huang, E. Lehmann, R.K. Puri, Nucl. Phys. A **548**, 102 (1992).
36. C. Fuchs, Amand Faessler, E. Zabrodin, Y.M. Zheng, Phys. Rev. Lett. **86**, 1974 (2001).
37. N. Ohtsuka, R. Linden, A. Faessler, F.B. Malik, Nucl. Phys. A **465**, 550 (1987); I. Izumoto, S. Krewald, A. Faessler, Nucl. Phys. A **341**, 319 (1980);
38. M. Baldo, I Bombaci, G. Giansiracusa, U. Lombardo, Phys. Rev. C **40** (1989) R491.
39. W. Zuo, I. Bombaci, U. Lombardo, Phys. Rev. C **60**, 024605 (1999).
40. F. de Jong, H. Lenske, Phys. Rev. C **54**, 1488 (1996).
41. G.Q. Li, R. Machleidt, Phys. Rev. C **48**, 2707 (1993).
42. H. Sorge, H. Stöcker, W. Greiner, Ann. Phys. (N.Y¿) **192**, 266 (1989).
43. S. Huber, J.Aichelin, Nucl. Phys. A **573**, 587 (1994).
44. Ch. Hartnack, R.K. Puri, J. Aichelin, J. Konopka, S.A. Bass, H. Stöcker, W. Greiner, Eur. Phys. J. A **1**, 151 (1998).
45. V.S. Uma Maheswari, C. Fuchs, Amand Faessler, L. Sehn, D. Kosov, Z. Wang, Nucl. Phys. A **628**, 669 (1998).
46. C. Fuchs, H.H. Wolter, Nucl. Phys. A **589**, 732 (1995).
47. FOPI Collaboration (V. Ramillien *et al.*), Nucl. Phys. A **587**, 802 (1995).
48. FOPI Collaboration (A. Andronic *et al.*) Nucl. Phys. A **661**, 333 (1999)c.
49. T. Gaitanos, H.H. Wolter, C. Fuchs, Phys. Lett. B **478**, 79 (2000).
50. FOPI Collaboration (P. Crochet), *XXXIV International Winter Meeting of Nuclear Physics*, edited by I. Iori (Bormio, 1996); FOPI Collaboration (N. Bastid *et al.*), Nucl. Phys. A **622**, 573 (1997).
51. W. Reisdorf, Nucl. Phys. A **612**, 493 (1997).
52. FOPI Collaboration (F. Rami *et al.*), Nucl. Phys. A **646**, 367 (1999).
53. E. Zabrodin, C. Fuchs, L.V. Bravina, A. Faessler, Phys. Rev. C **63**, 034902 (2001).
54. A.M. Poskanzer, S.A. Voloshin, Phys. Rev. C **58** 1671 (1998) 1671.
55. FOPI Collaboration (A. Andronic *et al.*), Phys. Rev. C **64**, 041604 (2001).
56. ALADIN Collaboration (T. Odeh *et al.*), Phys. Rev. Lett. **84**, 4557 (2000).
57. FOPI Collaboration (P. Crochet *et al.*), Nucl. Phys. A **624**, 755 (1997).
58. C. Pinkenburg *et al.*, Phys. Rev. Lett. **83**, 1295 (1999); P. Danielewicz, Roy A. Lacey, *et al.*, Phys. Rev. Lett. **81**, 2438 (1998).
59. KaoS Collaboration (C. Sturm *et al.*), Phys. Rev. Lett. **86**, 39 (2001).